Experimental study on the 3D-flow field of a free-surface vortex using stereo PIV

Duinmeijer, Alex; Oldenziel, Gosse; Clemens, Francois

DOI
10.1080/00221686.2018.1555558

Publication date
2020

Document Version
Final published version

Published in
Journal of Hydraulic Research

Journal of Hydraulic Research

ISSN: 0022-1686 (Print) 1814-2079 (Online) Journal homepage: https://www.tandfonline.com/loi/tjhr20

Experimental study on the 3D-flow field of a free-surface vortex using stereo PIV

Alex Duinmeijer PhD Student, Gosse Oldenziel Research Engineer, Researcher & Francois Clemens Professor

To cite this article: Alex Duinmeijer PhD Student, Gosse Oldenziel Research Engineer, Researcher & Francois Clemens Professor (2019): Experimental study on the 3D-flow field of a free-surface vortex using stereo PIV, Journal of Hydraulic Research, DOI: 10.1080/00221686.2018.1555558

To link to this article: https://doi.org/10.1080/00221686.2018.1555558

Published online: 15 Jan 2019.

Journal of Hydraulic Research, 2019
https://doi.org/10.1080/00221686.2018.1555558

Research paper

Experimental study on the 3D-flow field of a free-surface vortex using stereo PIV

ALEX DUINMEIJER, PhD Student, *Water Management Department, Faculty of Civil Engineering and Geosciences, Delft University of Technology, Delft, The Netherlands*
Email: spa.duinmeijer@rotterdam.nl/s.p.a.duinmeijer@tudelft.nl (author for correspondence)

GOSSE OLDENZIEL, Research Engineer, Researcher, *Hydraulic Engineering Department, Deltares, Delft, The Netherlands; Laboratory for aero- and hydrodynamics, Faculty of 3Me, Delft University of Technology, Delft, The Netherlands*
Email: gosse.oldenziel@deltares.nl / g.oldenziel@tudelft.nl

FRANCOIS CLEMENS, Professor, *Water Management Department, Faculty of Civil Engineering and Geosciences, Delft University of Technology, Delft, The Netherlands; Hydraulic Engineering Department, Deltares, Delft, The Netherlands*
Email: f.h.l.r.clemens@tudelft.nl / francois.clemens@deltares.nl

ABSTRACT
In order to analyse the flow characteristics of free-surface vortexes and to validate the Burgers vortex model by using stereo particle image velocimetry, experiments are conducted in a 600 mm diameter vortex tank. Measured axial velocities indicate that 10–25% of the flow is transported through the vortex core. The velocity profiles show that the axial flow is concentrated in a domain bounded by two times the core radius. Despite Burgers' assumption of radially independent axial velocity profiles, the model quantifies the tangential velocity profile within a relative uncertainty of circa 10%. The measurements show that it seems valid to use Burgers' model to obtain an estimate for the core radius by taking the average axial velocity over a radial domain of approximately 2.2 times the core radius. The Burgers model quantifies the air core depth with an uncertainty of 20% relative to the measurements. When compared with the magnitude of vorticity diffusion by molecular viscosity, the experiments show that there is no significant diffusion by radial turbulence.

Keywords: Air core depth; axial vortex flow; Burgers vortex model; experiments; stereo particle image velocimetry (SPIV); vortex dynamics; vortex core radius

1 Introduction

Wastewater pumping stations often experience problems due to the accumulation of individual floating particles of fat, oil and grease (FOG) in the pump sump. The presence of FOG can result in pump failures that may cause up to a 16% increase of yearly volume of combined sewer overflows, as shown by Korving, Clemens, and van Noortwijk (2006) for a specific case study. The current, widely accepted, guidelines for sump design (e.g. American National Hydraulic Standards Institute, 2012) only deal with the transport of floating debris in a superficial manner and for a limited number of sump geometries only. In order to obtain a more fundamental understanding of the FOG problems related to wastewater pumping stations, the authors initiated a research project to study the ability of free-surface vortices (hereafter referred as "vortex") as a mechanism to transport floating FOG particles from the water surface to the pump suction inlet (Duinmeijer & Clemens, 2016). An experimental set-up is constructed to study this transport ability for experimental particles having characteristic lengths of in the range of 0.02–0.04 m. Based on preliminary experiments, it was shown that the transport ability in both radial and axial direction strongly depends on the three dimensional flow field (3D-flow) in the vortex's irrotational flow field (outer field) and rotational flow field (vortex core) (Duinmeijer & Clemens, 2016). For example, particles could be ejected out of the vortex air core (irrotational field) due to an imbalance between the (hydrostatic) pressure forces

Received 22 November 2017; accepted 27 November 2018/Currently open for discussion.

ISSN 0022-1686 print/ISSN 1814-2079 online
http://www.tandfonline.com

and particle centrifugal force. Another observed phenomenon is that the particle can be "caught" in the vortex core due to an imbalance between the downward drag force generated by the vortex core axial velocity and the upward particle buoyancy force.

1.1 *Problem definition*

To predict the vortex's transport capacity, it is essential to obtain knowledge of the 3D-flow in both the vortex core and outer field. Furthermore, as air entrainment by an air core that extends into the pump must be prevented in the practical application of the vortex, there is a need for a reliable quantification of the vortex air core depth H_D. Over recent decades numerous research projects on the characteristics of vortex flow field have been reported. A part of the literature focuses on deriving the governing parameters and the effects of viscosity and surface tension on the vortex formation, e.g. Anwar (1966), Anwar, Weller, and Amphlett (1978), Dagget and Keulegan (1974), Rindels and Gulliver (1983) and Suerich-Gulick, Gaskin, Villeneuve, and Parkinson (2014a). Other research focuses on deriving expressions to compute the minimum submergence depth above an intake needed to prevent air entrainment by an air core extending into the pump, e.g. Anwar and Amimilett (1980), Odgaard (1986), Gulliver and Rindels (1987). Yet another area of research is in validating vortex models using experimental data, e.g. Hite and Mih (1994), Wang, Jiang, and Liang (2011) and Sun and Liu (2015). Nevertheless, only limited accurate experimental data are available on measurements of the 3D-flow in both the outer field and vortex core at different vertical positions and especially regarding the axial flow profile in the vortex core and its gradient in the vertical direction.

1.2 *Main research questions addressed*

To obtain knowledge on the vortex 3D-flow, the research questions addressed here are: (1) What is the distribution of the vortex velocity components in the vortex core and outer field? (2) Can the Burgers (1948) vortex model be validated to enable the quantification of the vortex characteristics? (3) What is the ratio Q_v/Q between the axial vortex flow Q_v and total flow Q?

1.3 *Research outline*

The vortex 3D-flow field in the outer field and vortex core is measured in three horizontal planes using stereo particle image velocimetry (SPIV). A cylindrical coordinate system (r, θ, z) is applied where the flow field is presented in tangential (V_θ), radial (V_r) and axial (V_z) velocities. The measured profiles of V_θ, V_r and V_z are compared with the V_θ profile of the Burgers (1948) vortex model and with the V_z profiles proposed by Hite and Mih (1994) and Wang et al. (2011). In the vortex flow, the core radius r_c is a characteristic parameter illustrating the radial position of transition between the vortex core and outer field. Burgers developed a model (hereafter referred to as Burgers' model) to compute r_c with $r_c = 2(\nu/a)^{0.5}$ representing the ratio between axial vortex stretching and molecular viscous diffusion of vorticity with $a = \partial V_z/\partial z$ the stretching parameter and ν the kinematic viscosity. As Burgers' model assumes an unrealistic radially independent V_z profile ($\partial V_z/\partial r = 0$), the validity of this model is studied when the measured radially dependent V_z is modelled as a spatially average value $\bar{V}_z$. Furthermore, the accuracy of Burgers' model to predict H_D for the present set-up is examined.

First, this paper addresses the theoretical background of free-surface vortices and the Burgers model. In Section 3 the experimental set-up, the SPIV method and measuring programme are presented. In Section 4 the results obtained for the velocity profiles are described and the validity of Burgers' model to compute r_c and H_D are discussed.

2 The free-surface vortex and the Burgers vortex model

A free-surface vortex is characterized by a solid-body rotating core with vorticity and an outer field of irrotational flow without vorticity. The vorticity ω is defined as the curl of the velocity vector: $\boldsymbol{\omega} = \nabla \times \boldsymbol{V}$ and is related to the angular momentum of a fluid particle around its centre of mass. A two-dimensional model describing V_θ for both fields was proposed by Rankine (1858):

$$V_\theta = \Omega r = \frac{\Gamma}{2\pi}\frac{r}{{r_c}^2}(r < r_c)$$
$$V_\theta = \frac{\Gamma}{2\pi r}(r > r_c) \quad (1)$$

In which Ω is the angular velocity of the vortex core and r_c is the position of the transition between the vortex core and the outer field (Fig. 1). The flow circulation Γ is defined as the line integral of a velocity around a closed curve C; based on Stokes' theorem it represents the flux of the vorticity vector $\boldsymbol{\omega}$ through any surface area A bounded by the closed curve C:

$$\Gamma = \oint_C \boldsymbol{V}d\boldsymbol{s} = \iint_A \boldsymbol{\omega}\cdot\hat{n}dA \quad (2)$$

Consequently, a circulation on C has a region that contains vorticity. In the Rankine model this region is the vortex core with $\omega = 2\Omega$. (Fig. 1). Based on the Navier–Stokes equations, Burgers proposed a 3D-vortex model that describes a balance between intensification of vorticity (the vortex stretching) and viscous diffusion of vorticity (Fig. 1). Burgers' model is based on the equation of conservation of vorticity given by:

$$\frac{D\omega}{Dt} = (\boldsymbol{\omega}\cdot\nabla)\boldsymbol{V} + \nu\nabla^2\boldsymbol{\omega} \quad (3)$$

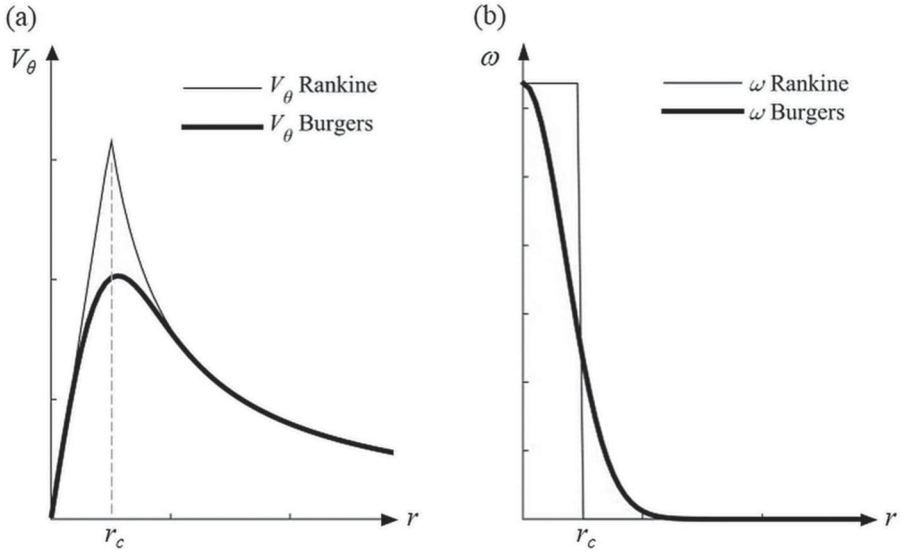

Figure 1 (a) Distribution of tangential velocity V_θ. (b) Distribution of vorticity ω. In the Rankine model, all vorticity is concentrated in the vortex core of solid-body rotation where the Burgers model shows viscous diffusion of vorticity

For an axi-symmetric flow there is only vorticity in z-direction allowing to reformulate Eq. (3) as:

$$\frac{\partial \omega_z}{\partial t} + V_r \frac{\partial \omega_z}{\partial r} + V_z \frac{\partial \omega_z}{\partial z} + \frac{V_\theta}{r} \frac{\partial \omega_z}{\partial \theta} = \omega_z \frac{\partial V_z}{\partial z} + \nu \left(\frac{\partial^2 \omega_z}{\partial r^2} + \frac{1}{r} \frac{\partial \omega_z}{\partial r} \right) \tag{4}$$

Without an external torque acting on the vortex and defining the terms $\partial \omega_z / \partial \theta = \partial \omega_z / \partial z = 0$ because of axi-symmetry and constant vorticity in z-direction, the vorticity is only a function of r:

$$V_r \frac{\partial \omega_z}{\partial r} = \omega_z \frac{\partial V_z}{\partial z} + \nu \frac{1}{r} \frac{\partial}{\partial r} \left(r \frac{\partial \omega_z}{\partial r} \right) \tag{5}$$

The first term of the right-hand side represents vortex stretching or extensional strain. To solve Eq. (5) with the boundary conditions $\omega_z(0)$ and $\omega_z(\infty)$, Burgers assumes an axial velocity profile that is independent of r and varies linearly with z:

$$V_z(z) = az, V_r(r) = -\frac{1}{2} ar \tag{6}$$

The profile of V_r is a result of conservation of mass. Using these profiles in Eq. (5) the following vorticity equation is obtained:

$$\frac{\partial \omega_z}{\partial r} = -\left(\frac{a}{2\nu} \right) r \omega_z \tag{7}$$

Integrating Eq. (7) gives the solution for the distribution of vorticity in radial direction:

$$\omega_z(r) = \omega_0 \exp \left[-\left(\frac{r}{r_c} \right)^2 \right] \tag{8}$$

where $\omega_0 = \Gamma_\infty / (\pi\, {r_c}^2)$ the vorticity in the vortex centre and r_c is the core radius, presenting the ratio between axial stretching $a = \partial V_z / \partial z$ and molecular diffusion of vorticity:

$$r_c = 2(\nu / a)^{0.5} \tag{9}$$

Applying Stokes' theorem on Eq. (8), the Burgers profile of V_θ is obtained:

$$V_\theta(r) = \frac{\Gamma_\infty}{2\pi r} \left\{ 1 - \exp \left[-\left(\frac{r}{r_c} \right)^2 \right] \right\} \tag{10}$$

It is noted that Burgers' assumption that $\partial V_z / \partial r = 0$ seems not valid for real vortices in the far flow field, but may hold in the direct vicinity of the core. This is discussed in Section 4.5. Various authors, e.g. Vatistas (1989), Mih (1990), Wang et al. (2011) and Sun and Liu (2015), proposed expressions based on Eq. (10) without the exponential term and using a dimensionless radius $R = r/r_c$.

3 Experimental set-up and programme

3.1 *Experimental set-up*

The experimental set-up consists of a cylindrical acrylic tank with an inside diameter of 0.610 m and a height of 1 m (Fig. 2). The tank is placed in a square 0.699 × 0.699 × 1.0 m acrylic container filled with water to reduce the effects of light refraction when recording camera images. The set-up is a closed loop system with a pump discharging water in the tank that flows through an outlet in the bottom back to the pump. The flow rate Q is measured with a Kobold type DMH magnetic-inductive flow meter (calibrated before the experiments, the average deviation was determined to be 2%) located in the pressure line at a distance $> 10d$ from any pipe components with d the component diameter. Two outlet pipe diameters (D = 0.030 m and

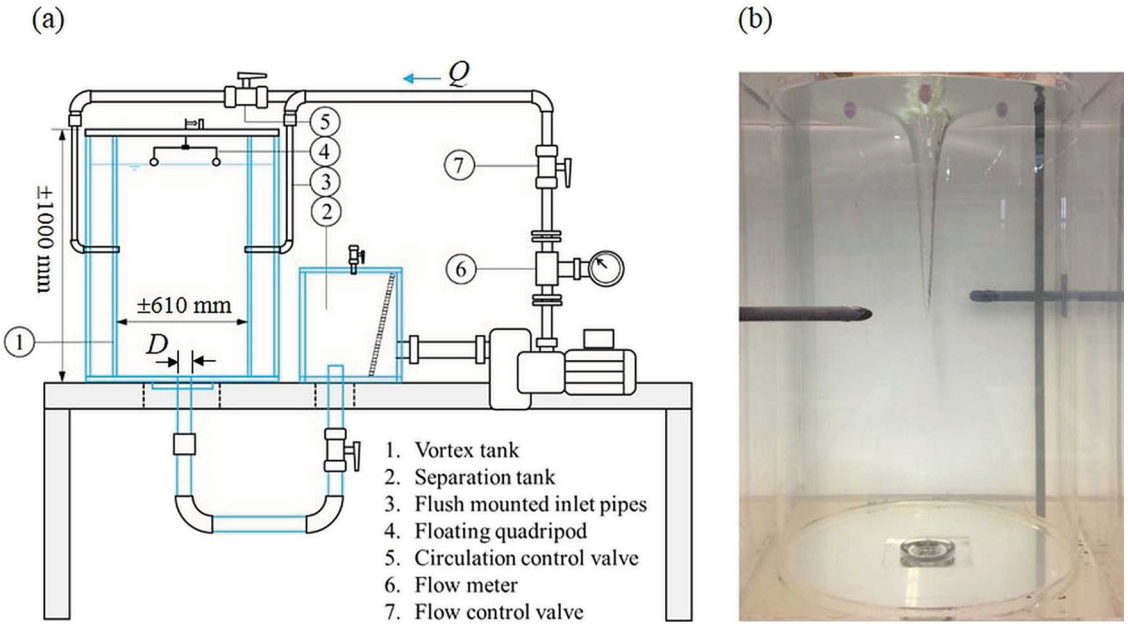

Figure 2 (a) Schematic overview experimental set-up. (b) Vortex tank with inlet pipes and floating quadripod

0.044 m) enable variation of the vortex characteristics by changing the mean outlet velocity $U_o = 4Q/\pi D^2$. The uncertainty in U_o is determined to be $\pm$ 0.01 m s^{-1}. The transition between tank bottom and outlet is curved to minimize flow separation and at the same time avoiding an error in the calculation of U_o. A separation tank of 0.3 $\times$ 0.3 $\times$ 0.4 m is placed between the tank outlet and the pump suction side for separating experimental floating particles from the closed system. The flow enters the tank through two horizontal Ø25.9 $\times$ 1.9 mm inlet pipes mounted flush in the tank wall placed 0.5 m above the tank bottom. The circulation Γ is determined with a floating quadripod. This device consists of four egg shaped floaters connected to a 0.30 m cross shaped frame of 3 mm diameter aluminium rods. The frame centre was connected to a vertical aluminium rod to centre the quadripod above the tank. This method was also applied by e.g. Brocard, Beauchamp, and Hecker (1983) and Echávez and McCann (2002). The circulation Γ is determined by measuring V_θ around a circle with diameter d:

$$\Gamma = \oint_C \mathbf{V}\mathrm{d}\mathbf{s} = 2\pi r V_\theta = \pi^2 d^2 N t^{-1} \tag{11}$$

with $d = 0.3$ m the length of the quadripod and t the measured time to accomplish N revolutions. The revolution rate N/t of the quadripod was recorded using a stopwatch. The measurement of Γ is done at a distance $r = 0.15$ m which is equal to $8r_c$ and thus larger than $3r_c$ which is assumed to be the minimum to measure the bulk circulation Γ_∞ (Suerich-Gulick et al., 2014a). By applying the theory of error propagation on Eq. (11) and assuming the uncertainty as normal distributed, the circulation uncertainty $\delta\Gamma = (\pi d)^2 (t/N)^{-2} \delta t$ and varies from 0.005 to 0.02 m^2 s^{-1}. The depth of the air core is measured using a stylus placed in the centre of the air core with an estimated uncertainty of $\pm$ 0.5 cm for series 1 to 3, $\pm$ 1 cm for series 4 to 6 and $\pm$ 2 cm for series 7 to 8. The uncertainty of this measurement is largely due to the oscillating behaviour of the air core depth and the water free-surface. Application of alternative methods like a video camera would probably yield the same uncertainty. During the experiments, the water temperature is measured and was found to vary between 22 and 28°C, influencing the physical properties of water such as viscosity and surface tension.

Influence of scale effects

The order of magnitude of the dimensions of the set-up are roughly similar to sumps of real wastewater pumping stations (the majority of wastewater pumping stations in the Netherlands are relatively small). Therefore, scale effects when translating the presented results to the application of vortices in real sumps are considered of minor importance.

3.2 *Stereo particle image velocity method and vector processing*

Stereo PIV measurement set-up

The stereo PIV set-up comprises two cameras (LaVision Imager MX 4M, Göttingen, Germany) imaging a horizontal plane covering approximately one quadrant of the inner tank cylinder. One camera captures the plane of interest from above and the other images the plane from below. The cameras pixel size is 5.5 μm at an image format of 2048 $\times$ 2048 pixels. Two 28 mm objectives (Nikon Nikkor, Minato, Tokio, Japan) are mounted on Scheimpflug adapters at the angle that yields the largest depth of field. Two acrylate water filled prisms are mounted on the tank to improve the imaging by reducing refraction effects. Nearest to the cameras the measurement plane is mapped onto the 10 bit CMOS sensor with a magnification of 0.079 and

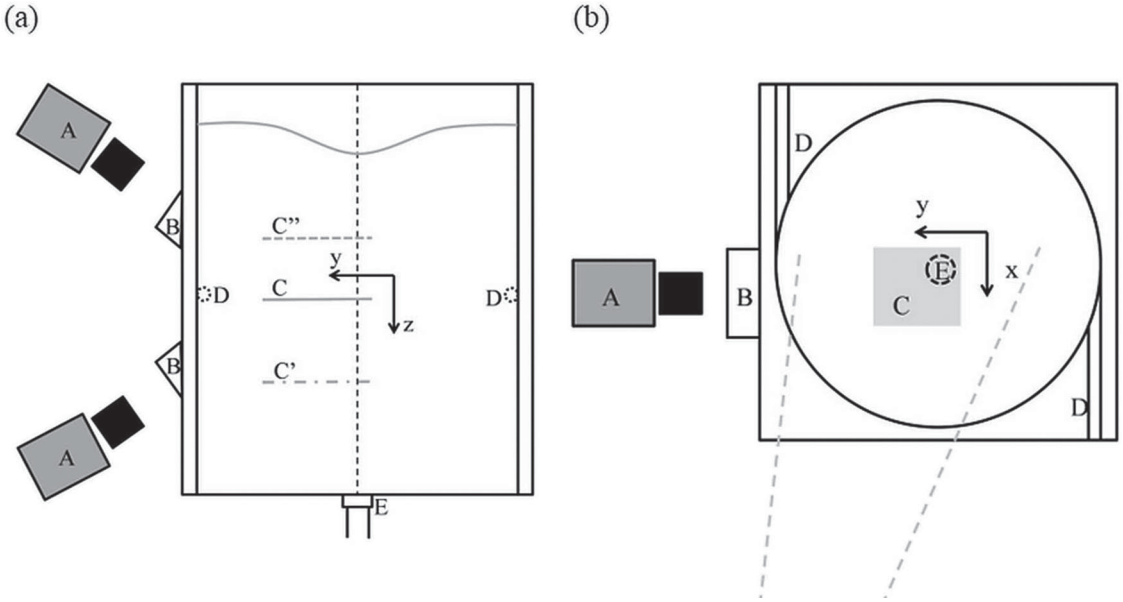

Figure 3 (a) (A) cameras, (B) water-filled prisms, (C) measurement area at height $h = 0.49$ m above tank floor (laser light sheet), (C′) measurement area at $h = 0.29$ m above tank floor, (C″) measurement area at $h = 0.62$ m above tank floor. (b) Top view of the set-up. (A) cameras, (B) water-filled prisms, (C) measurement area, (D) inlet pipes, (E) outlet. The grey lines indicate the width of the light sheet

furthest from the cameras the magnification is 0.10. Figure 3 shows a sketch of the set-up. To measure over a radial distance from the centre of the vortex that is as large as possible, the vortex core is positioned in a corner of the measurement domain. A pulsed laser (Litron lasers Nano L 50-100, Rugby, United Kingdom) at 532 nm and 50 mJ per pulse is used to generate a light sheet. For each measurement 500 image pairs are acquired at a sampling rate of 1 Hz. Stereo calibration for each plane is performed by placing a multilevel calibration target with round marks (LaVision, type 21) horizontally in the tank and using the third order polynomial method (Soloff, Adrian, & Liu, 1997). The light sheet is aimed at and aligned with the calibration plate. The stereo self-calibration correction is on the order of 0.01 pixel and 0.01°. The flow is seeded with 100 μm polyamide spheres (Vestosint, Evonik, Marl, Germany) with density $\rho = 1060\,\mathrm{kg\,m^{-3}}$. The particle seeding density is limited by the agglomeration of particulate matter in the core and is typically 10 particles per 64 × 64 pixel area.

Contour averaging method

To quantify V_θ over a large radial distance from the core, while resolving large gradients in velocity in the core, the SPIV results are contour averaged (CA) over an angle from 0 to $\pi/4$ radians. Figure 4 shows the area over which the CA over $\pi/4$ radians is applied. To obtain an average of V_z and V_r over a larger azimuthal domain near the core, a second CA is determined by averaging over a polar angle from $-\pi/2$ to π (Fig. 4b). Vectors inside the air core interface are excluded from analysis. The

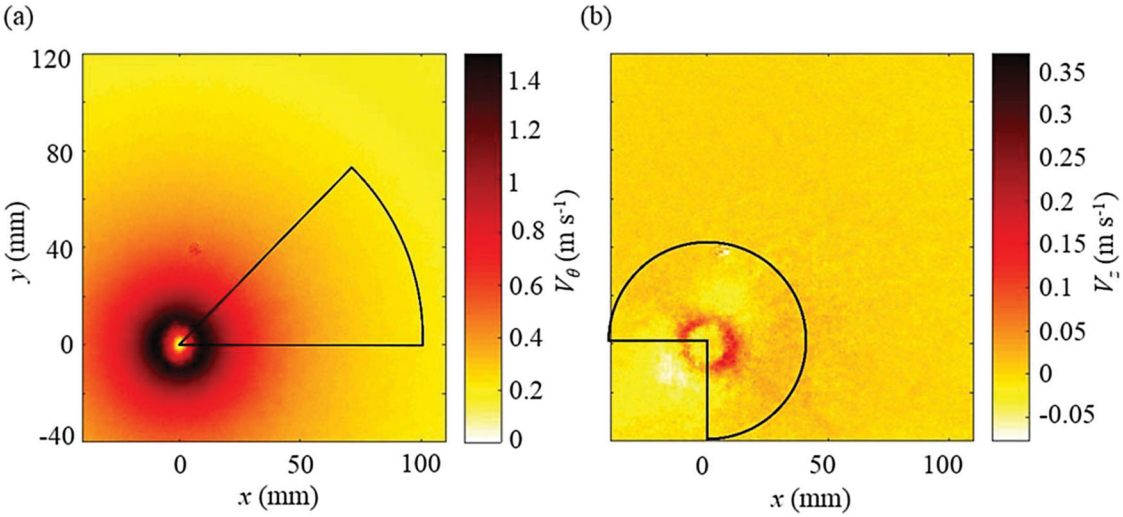

Figure 4 (a) V_θ of series 1 at $h = 0.29$ m. The area within the solid black line is the area in which CA is applied for the large domain. (b) V_z. The domain inside the black line is the area in which CA is applied for the azimuthal domain of $3\pi/2$ rad (V_z and V_r)

angular domain for the CA of V_z is selected larger than that used for the CA of V_θ to obtain an estimate of the axial mass flow at the cost of resolution of steep spatial gradients. The vortex centre location is obtained by calculating the location of maximum rotation from the in-plane SPIV vector field results. Vector fields are determined using the DaVis8 PIV software by LaVision. A background subtraction is performed and a mask is applied. In case the air core is present in the measurement plane the SPIV correlation procedure consists of a sum-of-correlation (SOC) approach over 500 double frame images with three passes at 64 × 64 pixel areas with 50% overlap followed by two passes at 32 × 32 pixel areas with 50% overlap (Meinhart, Wereley, & Santiago, 2000). Universal outlier detection is used for vector validation (Westerweel & Scarano, 2005).

The weighted conditional averaging method

Weighted conditional averaging over the core location is performed as described in Pennings, Westerweel, and Van Terwisga (2015) in case the air core is not present in the measurement plane. The procedure of weighted conditional averaging of SPIV data consists of the following steps. (1) Conventional SPIV processing is performed at a coarse resolution (48 × 48 pixels using 50% overlap for every double frame image). From the in-plane velocity vectors the core location is determined by fitting a parabola to the sum of the absolute values of the vertical and horizontal components. (2) The raw data files with similar vortex locations are grouped and SOC processing is applied to the separate groups. (3) The SOC processing results of these groups are then weighted by the number of raw data images used in the group versus the total number of used images and summed. Using this approach, a higher spatial resolution can be attained. In the present work, the maximum spatial resolution is 8 × 8 pixels with 50% overlap which gives a vector spacing of 0.39 mm.

3.3 *Measuring programme*

The measuring programme to measure r_c, V_θ, V_r and V_z consisted of eight series. Series one to four was conducted with $D = 0.03$ m and series five to eight were conducted with $D = 0.044$ m. All experiments were conducted with an undisturbed water depth H of 0.90 m. The quantities were measured at three horizontal planes at $h = 0.29$, 0.49 and 0.62 m measured from the tank bottom. The range of experimental hydraulic conditions D, Q and Γ were selected to generate vortices with air core depths in the range of 0.09 m to 0.85 m. The selected flow rates resulted in two equal U_o values for four series. This condition was selected to study the relation between U_o and r_c as discussed later. All four series consisted of measurements with two flow rates and with two different Γ for each flow rate. Γ was changed by using one or both inlet pipes. Table 1 shows the measurement series and Γ_{quad} with 95% confidence interval determined by the quadripod.

4 Results and discussion

4.1 *Measured circulation*

Based on Eq. (11), Fig. 5 shows the Γ of both the floating quadripod (Γ_{quad}) and SPIV measurements (Γ_{SPIV}) for all series. The Γ_{SPIV} is plane averaged and determined at $r = 0.135$ m. Γ_{quad} includes the 95% confidence interval ($\pm 2\sigma$) due to uncertainties in the measured parameters. For the presented research purposes, Γ_{quad} shows a sufficiently close match to Γ_{SPIV}. Differences between both methods can be explained by the observation that the Γ_{SPIV} shows a minor gradient in the radial direction indicating that the outer field is not entirely irrotational. This was also observed in the PIV measurements of Sun and Liu (2015). There is a radial variation as well in Γ_{SPIV} due to the concentrated momentum influx from the Ø25.9 mm inlet pipes. This causes a slightly non-uniform distribution of angular momentum along the radial direction throughout the outer field.

4.2 *Measured velocity profiles*

The measured velocity profiles are analysed for measurements with no air core crossing a measurement plane only. Because

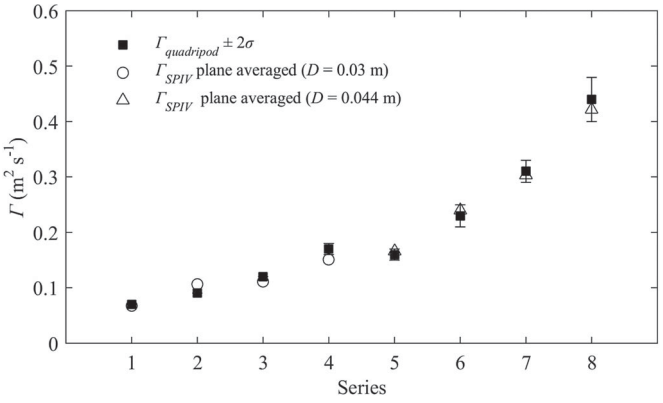

Figure 5 Γ measured by quadripod at $r = 0.15$ m and by SPIV at $r = 0.135$ m. The error bars represent the 95% confidence interval

Table 1 Measurement series with hydraulic conditions and Γ_{quad}

Series	Q (m^3 h^{-1})	D (m)	Γ_{quad} (m^2 s^{-1})	Series	Q (m^3 h^{-1})	D (m)	Γ_{quad} (m^2 s^{-1})
1	0.69	0.030	0.07 ± 0.01	5	1.50	0.044	0.16 ± 0.01
2	0.69	0.030	0.08 ± 0.01	6	1.50	0.044	0.23 ± 0.02
3	1.16	0.030	0.12 ± 0.01	7	2.50	0.044	0.31 ± 0.02
4	1.16	0.030	0.17 ± 0.01	8	2.50	0.044	0.44 ± 0.04

of the different SPIV measurements post processing methods, V_r and V_z are shown for $0 < r < 0.04$ m and V_θ is shown for $0 < r < 0.10$ m.

Tangential velocity profiles

For series three and five (all other series produced roughly similar profiles) the measured velocities in each plane are shown in Fig. 6. The figure also shows Burgers' profile of V_θ (Eq. (10)) by using the measured Γ_∞ and r_c for that plane. For Γ_∞, the Γ_{SPIV} at $r = 3r_c$ is used where the vorticity is decreased to almost zero and the flow is assumed as irrotational (Suerich-Gulick, Gaskin, Villeneuve, & Parkinson, 2014b). The determination of the measured r_c is given in Section 4.4. For all series, the measured profiles of V_θ show only slight differences between the different planes. Indeed, for this axi-symmetric vortex, the assumption is that $\partial V_\theta/\partial z \sim 0$ as is shown by the PIV data of e.g. Sun and Liu (2015) as well and which characterizes the 2D line vortex. Burgers' profiles of V_θ match the measured profiles. However, for series five (and a few others) the model shows an underprediction of the maximum velocity. This is not related to the non-uniformity of Γ_{SPIV} in the outer field and postulating Γ_{SPIV} at $r = 3r_c$ as Γ_∞. The use of Γ_∞ calculated at $r = 5r_c$ gives no significant changes in maximum velocities. The deviations δV_θ are possibly related to a combination of (a) Burgers' assumption of a radially independent axial velocity and (b) the uncertainty of r_c. However, by defining a required accuracy $|\delta V_\theta/V_\theta| < 10\%$ for the presented research purposes, the Burgers model produces a sufficiently accurate prediction of the V_θ profile.

Radial velocity profiles

The analysis of the measured profiles of V_r was shown to be straightforward. Figure 6 shows that the velocities are relatively low (< 0.1 m s^{-1}) and are observed to be the same order as the uncertainties. Therefore, the analysis is limited to a qualitative description of the velocity profiles. The velocities are negative representing radial inflow towards the vortex centre. The inflow is concentrated in a domain with radius comparable to the outlet radius with a maximum around r_c which was also showed by the PIV data of Sun and Liu (2015). The measured velocity profiles show some similarity with the model Einstein and Li (1951)

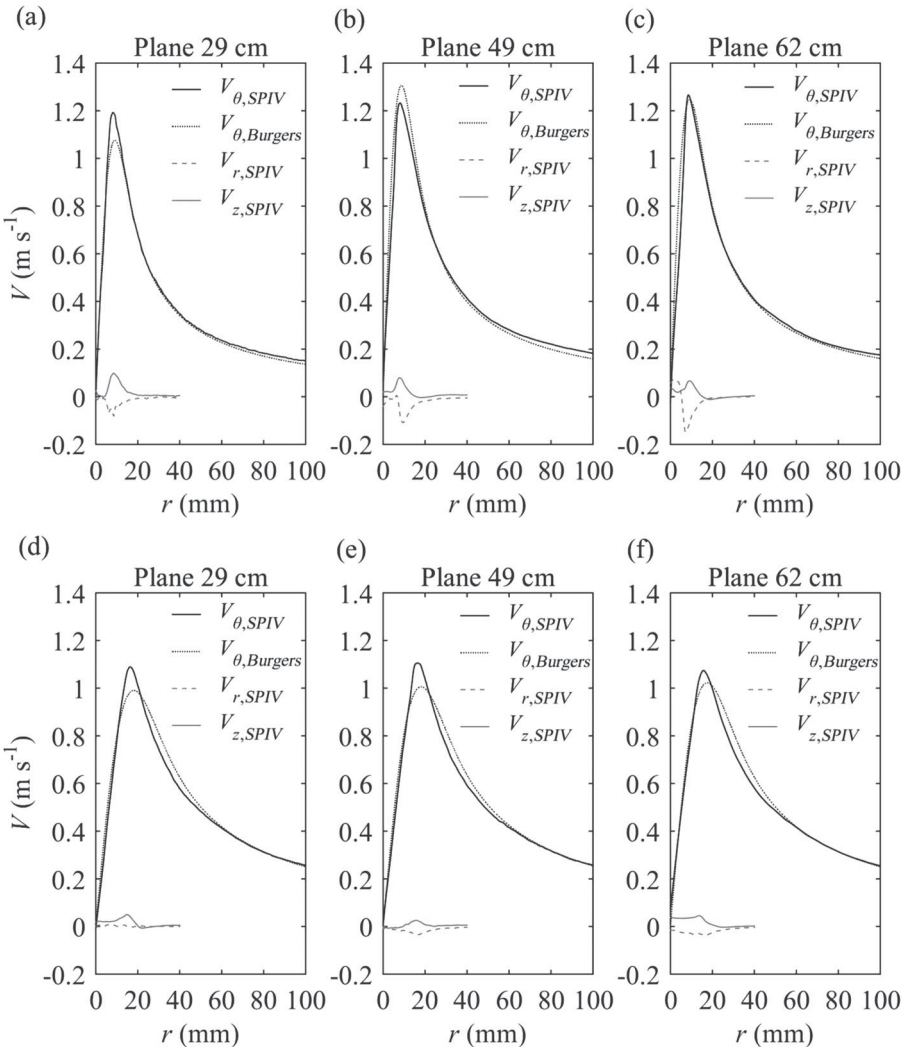

Figure 6 (a–c) Measured profiles of V_θ, V_r and V_z for series 3 with $D = 0.03$ m. (d–f) Measured profiles for series 5 with $D = 0.044$ m. The graphs include Burgers' profile of V_θ (Eq. (10)) using the characteristic parameters Γ_∞ and r_c

proposed, assuming axial plug flow bounded by a domain with radius α and $V_z = 0$ at $r > \alpha$:

$$V_r = \begin{cases} -\dfrac{qr}{2\pi\alpha^2}, r < \alpha \\ -\dfrac{q}{2\pi r}, r > \alpha \end{cases} \quad (12)$$

where $q = Q_v/H$. The vortex flow rate Q_v is defined as the axial down-flow. Unfortunately, a quantitative comparison with the measured profiles is not possible. V_r is found to be negligible compared to V_θ. This supports the choice that was made to neglect the V_r terms in the computation of H_D as discussed in Section 4.5.

Axial velocity profiles

For all series, the measured profiles show that the axial down-flow is primarily concentrated in a domain with a radius in the order of 2–3r_c while having a semi-parabolic profile with a maximum at r_c. A similar profile was observed in the experiments of Ito, Ezure, and Ohshima (2014). The maximum V_z is observed to be in a range of 4–8% of the maximum V_θ. The measured velocity profiles are not in line with the V_z models of e.g. Hite and Mih (1994) and Wang et al. (2011). These models suggest that the maximum V_z occurs at the axis of symmetry. However, the models mentioned were validated using experimental data available for $r > r_c$ only, while no data were available for model validation of the vortex core region. In order to ensure mass conservation, the V_z profile should show a positive gradient in the downward direction ($\partial V_z/\partial z > 0$). As V_r is assumed to be constant in the axial direction, the gradient is constant and thus V_z follows a linear profile along the vortex length. The gradient is not clearly visible for series one and two because the differences in V_z between the planes are very small and in the same order of magnitude as the measurement uncertainties. The uncertainty for these series are assumed to be 0.2–2% of the maximum value of V_θ (Westerweel & Scarano, 2005).

Secondary flow patterns

The measured V_z profiles do not show any significant velocities in the outer flow field ($r > 3r_c$). Consequently, secondary flow patterns in the outer field as observed by e.g. Echávez and McCann (2002) are not expected. However, a reliable statement on the absence of (small) secondary flow patterns cannot be made, as the very small velocities in the outer field are in the same order of magnitude as the measurement uncertainty.

4.3 *Axial vortex flow*

For each plane the axial vortex flow Q_v is determined by integration of the V_z profile over the cross-sectional area A:

$$Q_v(z) = \iint_A V_z(r)\mathrm{d}A = 2\pi \int_0^r V_z(r) r \,\mathrm{d}r \quad (13)$$

where A is the area containing all axial flow bounded by r. The integration boundary is defined in terms of r_c and set to $2.2r_c$ to use the largest number of available measured values of V_z. Figure 7 shows the computed ratios Q_v/Q for the planes 0.29 and 0.49 m. The Q_v/Q of series four and plane 0.49 m is considered as an outlier because of hindered optics due to agglomeration of particulate contamination in the vortex core just below the air–water interface. All measurements show distinctly that the vortex carries only a small percentage of the discharge Q. This is in line with the experimental observations made by Echávez and McCann (2002) and Andersen, Bohr, Stenum, Rasmussen, and Lautrup (2006). By assuming a linear gradient in vortex flow between the planes, Q_v at the tank bottom is quantified by extrapolation of the obtained values of Q_v between the planes 0.62 and 0.29 m to the tank bottom. Figure 7h shows that Q_v at the tank bottom falls in a range of 10–25% of Q. Furthermore, there is no clear relation observed between the maximum Q_v/Q and the discharge Q or outlet diameter D.

4.4 *Validation of the Burgers model to compute the core radius*

Vortex core radius

The validation of Burgers' model to compute r_c is based on the experimentally observed r_c. This r_c is taken equal to the radial position where the measured V_θ is maximal ($V_{\theta-\max}$). For each series, r_c is assumed to be normally distributed and presented as $\bar{r}_c \pm \sigma_c$, where $\bar{r}_c$ is the mean value of the three planes and σ_c the standard deviation. A Student's t-test shows less than 5% significance for each mean radius $\bar{r}_{c,p} \pm \sigma_{c,p}$ of each plane constructed by the 95% confidence interval of measured velocities around $\bar{r}_{c,p}$ where $V_\theta(r) + 2\sigma_{v\theta} < V_{\theta-\max}$. When the air core intersects a measurement plane, the radius is not considered in the calculation of $\bar{r}_c$ except for series eight in which the air core diameter was smaller than r_c. For series seven to eight, σ_c is taken equal to the standard deviation of the 95% interval as the velocities are only measured for one plane. Figure 8 shows $\bar{r}_c$ including the 95% confidence interval.

Relation between U_o and r_c

Figure 8 shows that there is no unique relation between the average outlet velocity U_o and r_c. Using only U_o to compute r_c seems invalid, as does Odgaard's (1986) model to predict the submergence depth S by using $r_c = 2(\nu_{eff}/a)^{0.5}$ with $a = \partial V_z/\partial z = U_o/H$. Odgaard (1986) proposes that an increase in circulation leads to high radial shear stresses near the vortex core that generates turbulence which increases diffusion of vorticity. Therefore, to include the diffusion of vorticity by radial turbulence, Odgaard introduced an effective viscosity $\nu_{eff} = \nu + k\Gamma_\infty$ with $k\Gamma_\infty$ the eddy viscosity and k the factor of proportionality given by $k = 6 \times 10^{-5}$ for a typical experimental set-up. For the research presented here, the Reynolds number R is in a range between 8×10^3 and 2×10^4

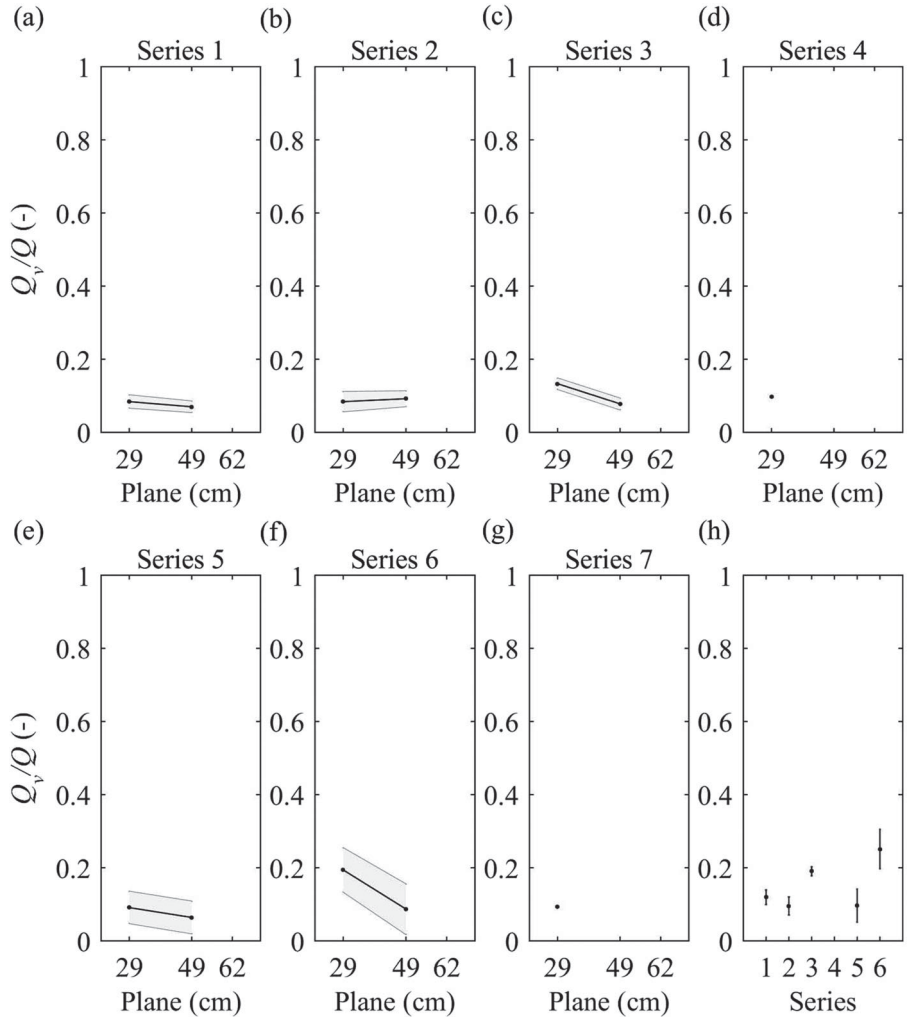

Figure 7 (a–g) ratio between axial vortex flow Q_v and total flow Q for the measurement planes $h = 0.29$ and $h = 0.49$ m. (h) Approximation of Q_v/Q at tank bottom ($h = 0$ m). All values include the 95% confidence interval

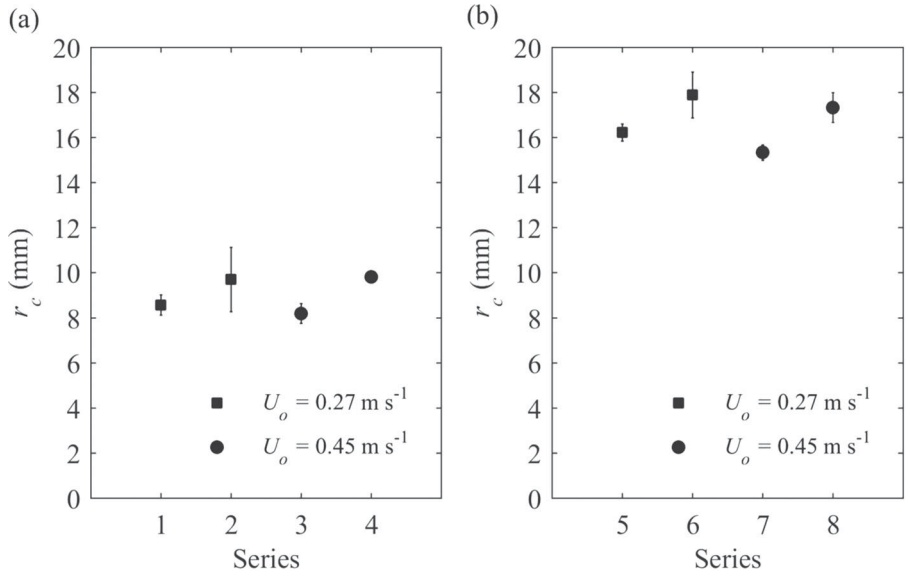

Figure 8 (a) Plane averaged $\bar{r}_c$ obtained from location of maximum V_θ including the 95% confidence interval for series $D = 0.03$ m. (b) $\bar{r}_c$ for series $D = 0.044$ m

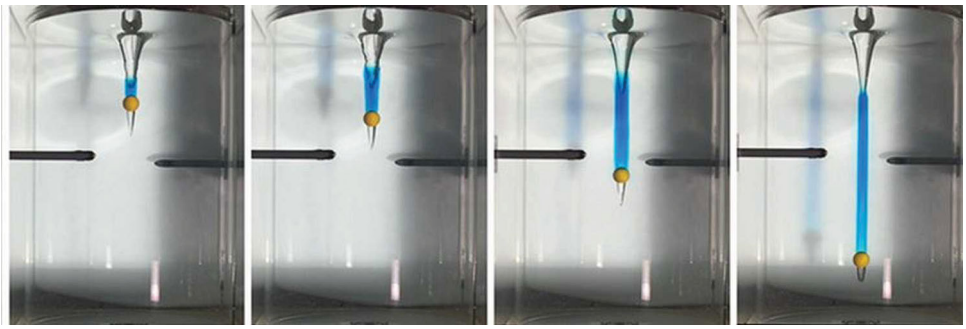

Figure 9 Experiment of slow axial transport of a Ø50 mm sphere in a vortex with $r_c \approx 17$ mm where dye is injected into the vortex core above the sphere. The dye core shows no radial diffusion of dye towards the outer field and thus no indication of radial turbulence

with R defined by $V_\theta\ r_c/\nu$. In this range, radial turbulence can be present. However, the results presented here show that the occurrence of radial turbulence around the vortex core is uncertain, as shown by Fig. 9 where no radial diffusion of dye is observed. Suerich-Gulick et al. (2014a, 2014b) propose a semi-empirical model to determine r_c from the approach flow and the geometry of a specific laboratory-scale hydropower intake based on Burgers' model of $r_c = 2(\nu\ /a)^{0.5}$. The experimental results reported by Suerich-Gulick et al. (2014a, 2014b) match with Burgers' model without using eddy viscosity. These results suggest that eddy viscosity is used to compensate the undecided use of U_o to predict r_c. For a similar type of experimental set-up as that presented here, Sun and Liu (2015) propose an expression where r_c is only a function of $\Gamma_\infty : r_c = 1.69T_\infty^{0.55}$. However, as Γ_∞ strongly depends on Q, Sun and Liu (2015) show also a relation between Q and r_c. Using the equation suggested by Sun and Liu (2015) with the measured Γ_∞ presented here, and comparing the thus determined r_c with the measured r_c, shows significant deviations. Consequently, relations between vortex characteristics appear to be highly dependent on the geometry of the experimental set-up used.

Validation of Burgers' model when using radially dependent V_z profiles

Burgers' model of $r_c = 2[\nu\ /(\mathrm{d}V_z/\mathrm{d}z)]^{0.5}$ is derived using the assumption of a radially independent V_z profile given by $V_z = az$. The measured V_z profiles show that this assumption not valid. In this section, the validity of this model is studied for radially dependent V_z profiles comparable to the present measurements of V_z. To do this, the measured V_z profile is converted to a radially independent average velocity $\bar{V}_z$ which is used in Burgers' model for r_c. $\bar{V}_z$ is computed based on the vortex axial flow Q_v:

$$\bar{V}_z = \frac{\iint_A V_z(r)\mathrm{d}A}{A} = \frac{Q_v}{\pi\,(2.2r_c)^2} \tag{14}$$

with A bounded by $r = 2.2r_c$. Assuming the V_z profile linear with z, the gradient $\mathrm{d}\bar{V}_z/\mathrm{d}z$ is then computed by using the average gradient of $\mathrm{d}Q_v/\mathrm{d}z$ between the planes:

$$\frac{\mathrm{d}\bar{V}_z}{\mathrm{d}z} = \frac{1}{n-1}\sum_{i=1}^{n-1}\left\{\frac{1}{[h(i+1)-h(i)]} \times \left[\frac{Q_v(i)}{\pi\,(2.2r_{c,i})^2} - \frac{Q_v(i+1)}{\pi\,(2.2r_{c,i+1})^2}\right]\right\} \tag{15}$$

with $Q_v = (Q_{v,0.29}, Q_{v,0.49}, Q_{v,0.62})$ and $h = (0.29\text{ m}, 0.49\text{ m}, 0.62\text{ m})$ and n the number of planes where Q_v is measured. By substituting Eq. (15) in Burgers' model of r_c, the following expression is obtained to compute r_c with the Burgers model:

$$r_c = 2\sqrt{\nu\left(\frac{1}{n-1}\sum_{i=1}^{n-1}\left\{\frac{1}{[h(i+1)-h(i)]}\left[\frac{Q_v(i)}{\pi\,(2.2r_{c,i})^2} - \frac{Q_v(i+1)}{\pi\,(2.2r_{c,i+1})^2}\right]\right\}\right)^{-1}} \tag{16}$$

Figure 10a shows the computed r_c for series one, two, three, five and six (for series five the gradient is used between the planes 0.29 and 0.49 m). The determined value for r_c for the series three, five and six show a match with the measured r_c, while series one and two show a deviation of circa 60%. These deviations are possibly related to the small axial velocity differences between the planes with the same order of magnitude as the measurement uncertainty. Another explanation could be the presence of a Taylor–Proudman column above the outlet, suppressing axial velocity gradients. The typical Rossby number $\mathrm{R_o} = V_\theta(r_c)/2\Omega\ r_c$ for this set-up is circa 0.5, indicating that the Coriolis forces are of the same order of magnitude as the inertial forces. However, a further discussion on this phenomenon is beyond the scope of this study. To conclude, it seems valid to use Burgers' model for the estimation of r_c by taking the gradient of the average value $\bar{V}_z$ of the radially dependent V_z profile within the vortex and assuming it to be linear. Figure 10b shows the results of the computed r_c if extra diffusion of vorticity due to radial turbulence is applied as proposed by Odgaard (1986) where ν is replaced by $\nu + k\Gamma_\infty$ with $k = 10^{-5}$ to use an eddy viscosity in the same order of magnitude as the kinematic viscosity. Indeed, as radial turbulence is likely to be absent, the

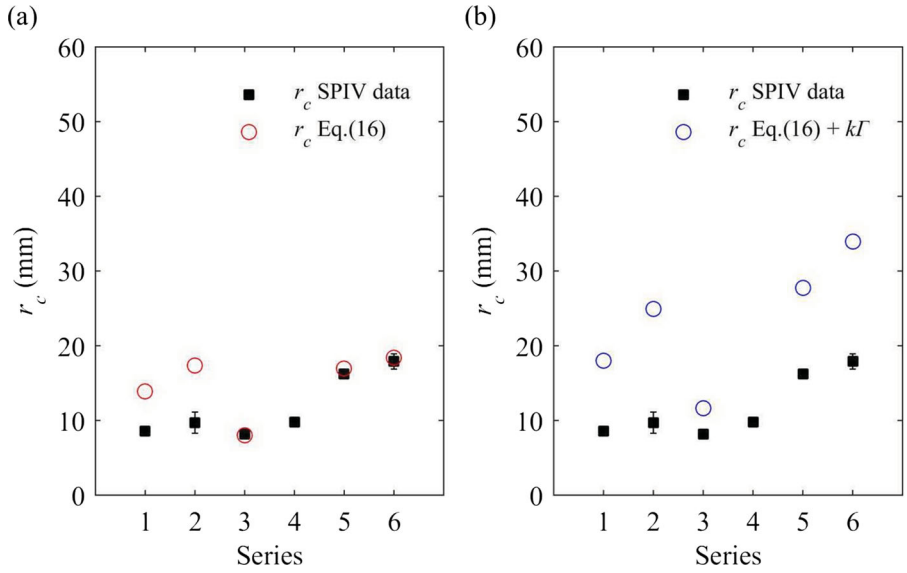

Figure 10 (a) Comparison of measured and computed r_c using $\bar{V}_z$. (b) Comparison including extra diffusion of vorticity by radial turbulence with $k\Gamma$ of the same order of magnitude as the kinematic viscosity

introduction of a small eddy viscosity leads to unrealistic large values of the core radii.

4.5 *Computation of H_D with the Burgers model*

The computation of H_D or total surface depression is based on conservation of radial momentum from the Navier–Stokes equations by assuming $\partial V_r/\partial z = 0$ and neglecting the contribution of the V_r terms since they are very small compared to the V_θ terms as shown in Section 4.2. The radial pressure term as a function of r is then:

$$p(r) = \rho \int_0^r \left[\frac{V_\theta^2}{r} - V_r \frac{\partial V_r}{\partial r} + \nu \frac{\partial}{\partial r}\left(\frac{\partial V_r}{\partial r} + \frac{V_r}{r} \right) \right] \mathrm{d}r \approx \rho \int_0^r \frac{V_\theta^2}{r} \mathrm{d}r + p(0) \tag{17}$$

and characterizes the balance between radial pressure force and centrifugal force of the rotating fluid. The pressure distribution in the axial direction is determined by taking the integral of the axial Navier–Stokes equations and neglecting the V_z pressure terms as they are small compared to the pressure due to the gravitational force:

$$p(r) = \rho \int_0^z \left[V_r \frac{\partial V_z}{\partial r} + V_z \frac{\partial V_z}{\partial z} + \nu \left(\frac{\partial^2 V_z}{\partial r^2} + \frac{1}{r}\frac{\partial V_z}{\partial r} + \frac{\partial^2 V_z}{\partial z^2} \right) - g \right] \mathrm{d}z \approx p(0) - \rho g z \tag{18}$$

Consequently, the pressure distribution is taken as hydrostatic as supposed by e.g. Odgaard (1986), Gulliver and Rindels (1987), Hite and Mih (1994) and Andersen et al. (2006). When including surface tension, the elevation h of the free surface is approached by:

$$h(r) = h(0) + \frac{1}{g}\rho \int_0^r \frac{{V_\theta}^2}{r} \mathrm{d}r - \frac{\sigma}{\rho g}[\kappa(r) - \kappa(0)] \tag{19}$$

with σ the fluid surface tension and κ the surface curvature (Andersen et al., 2006):

$$\kappa(r) = \frac{h'}{r[1 + (h')^2]^{1/2}} + \frac{h''}{[1 + (h')^2]^{3/2}} \tag{20}$$

with $h' = \mathrm{d}h/\mathrm{d}r$ and $h'' = \mathrm{d}^2h/\mathrm{d}r^2$. Subsequently, H_D, or the total surface depression, is approached by integrating Eq. (19) between $r = 0$ and $r \to \infty$ while neglecting the curvature $\kappa(\infty)$ at infinity:

$$H_D = h(\infty) - h(0) = \frac{1}{g}\int_0^\infty \frac{V_\theta^2}{r}\mathrm{d}r - \frac{\sigma}{\rho g}\kappa(0) \tag{21}$$

Influence of surface tension

The influence of surface tension σ on H_D has been studied by many authors. For example, Anwar et al. (1978) stated that the influence of σ can be neglected when the Weber number $\mathrm{We} = \rho {U_o}^2 H/\sigma > 10^4$. In our experimental range with $\sigma = 0.072\,\mathrm{N\,m^{-1}}$ (25°C), We varies between 10^3 to $3{\cdot}10^3$, implying that σ cannot be neglected; however, the relative contribution is unknown. Odgaard (1986) states that the surface tension pressure p_s at the tip of the air core is of a magnitude of $-2\sigma/r_c$, giving a maximal contribution to the presented experimental range of circa 1% of the measured H_D. Suerich-Gulick et al. (2014b) numerically examined the relative contribution of surface tension $\delta = (h_n - h_\sigma)/h_n$ on the air core depth for different scales and shapes of the surface depression as a function of the nominal slope $\zeta = h_n/r_c$, where h_n and h_σ are the calculated H_D without and with σ. For funnel-shaped air cores

Figure 11 Free-surface vortex air core depths H_D for series 5 to 8 with from left to right: $H_D = \pm 0.17$ m, ± 0.26 m, ± 0.54 m and ± 0.85 m. All air cores are typically funnel shaped

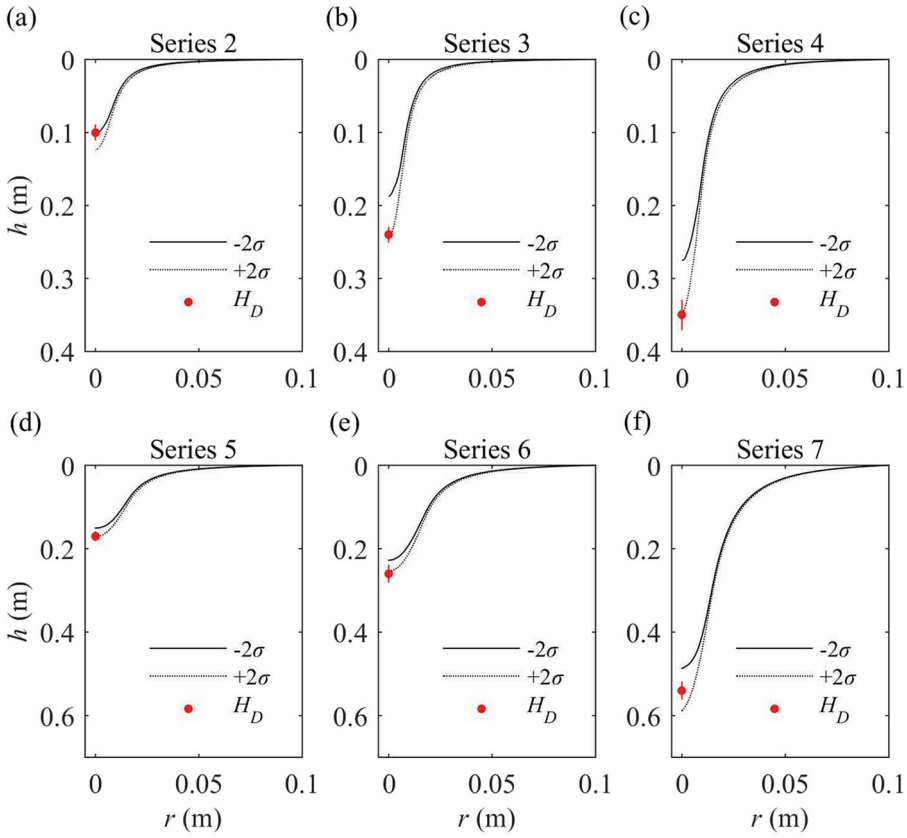

Figure 12 (a) to (f) Surface depression profile computed with Eq. (19) and without surface tension and compared with the measured H_D for series 2 to 7. Both results are presented with the 95% confidence interval

(Fig. 11) with a minimal nominal slope in our experimental range of about 10, Suerich-Gulick et al. (2014b) showed that the relative contribution has a maximum of about 2%. Because of this minor contribution, the influence of σ in the computation of H_D is neglected.

Validation of the expression to compute the surface elevation h(r)

The Burgers model to quantify H_D is based on the expression to compute the surface elevation (Eq. (19)) without taking surface tension into consideration. Therefore, both Eq. (19) and the assumption of negligible surface tension effects is validated by comparing the results of Eq. (19) with the measured H_D. The comparison uses the measurements of V_θ at plane $h = 0.29$ m. Figure 12 shows that Eq. (19) matches with measured H_D showing some under-prediction for most of the series that validates neglecting surface tension effects for the presented experimental range.

Computation of H_D with the Burgers model

The Burgers model to compute H_D is obtained by substituting Burgers' expression of V_θ in the validated Eq. (19) and integrating over $r \in [0, \infty]$ while neglecting effects due to surface tension:

$$H_D = \frac{1}{g}\int_0^\infty \frac{V_\theta^2}{r}\mathrm{d}r = \frac{\ln 2}{4\pi^2 g}\left(\frac{\Gamma_\infty}{r_c}\right)^2 \tag{22}$$

Figure 13 shows the results of the Burgers model using $\bar{\Gamma}_{SPIV}$ and $\bar{r}_c$ that are the plane averaged values. For series one to six, the Burgers model shown an under-prediction of H_D while there is an over-prediction of H_D for series seven and eight. The randomness of the deviations is probably related to a combination of minor inaccuracies in $\bar{r}_c$ and Burgers' assumption of an unrealistic radially independent V_z profile. To conclude, with an uncertainty of approximately 20% the Burgers model produces sufficiently accurate results for the research purposes addressed in this study.

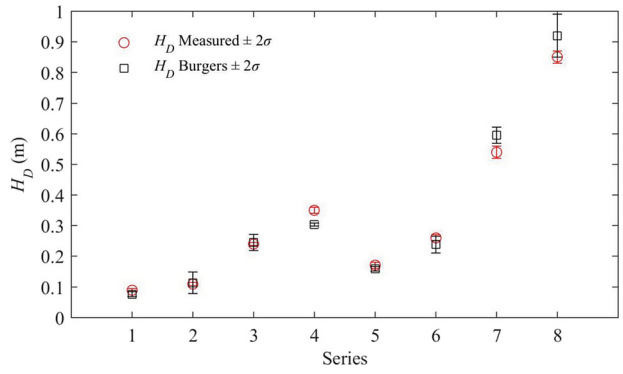

Figure 13 Computed air core depth H_D with the Burgers model (Eq. (22)) compared to measured H_D. Both results are presented including the 95% confidence interval because the averaged core radius $\bar{r}_c$ was used and because of uncertainty linked to air core tip instability

5 Conclusions

For a Ø600 mm vortex tank a unique set of velocity field measurements of the 3D-flow field of the free-surface vortex at different planes is presented including Γ_∞, the profiles of V_θ, V_r, V_z and r_c. The use of a simple floating quadripod to measure Γ proved to be a simple but accurate measuring device. The profile of V_θ is shown to be nearly independent of the vertical coordinate ($\partial V_\theta/\partial z \approx 0$) and thus the rotational flow can be assumed as a 2D line-vortex. Based on the characteristic vortex parameters r_c and Γ_∞, where Γ_∞ is assumed to be equal to Γ at $r = 3r_c$, the Burgers (1948) vortex model produces a sufficiently accurate estimate of the V_θ profile for the present research purposes. The profile of V_r was hard to measure because of the velocities being in the same order of magnitude as the measurement uncertainty. The radial inflow is primary concentrated near the vortex core with a maximum velocity around r_c and being zero in the outer field. For all series, the measured V_z profiles show that the axial down-flow is primary concentrated in a region with a radius comparable to approximately $2-3r_c$ while showing a semi-parabolic profile with a maximum around r_c. Integration of the measured V_z shows that between 10% and 25% of the flow is transported by the vortex. The measurements show that it is valid to use Burgers' model for the computation of r_c for radially dependent V_z profiles by using the average $\bar{V}_z$ over a radial domain of $2.2r_c$. Compared to the magnitude of diffusion of vorticity by molecular viscosity, the experiments show that there is no considerable diffusion by radial turbulence. The influence of surface tension can be neglected in the computation of H_D for the present experimental range. By only using Γ_∞ and r_c and compared with the measured H_D, the Burgers model computes H_D with an uncertainty of 20%. The purpose of the vortex' application is to transport floating debris to the pump suction inlet. At the design stage, there is a safety margin in distance between H_D and the inlet depth as air entrainment by a full air core must be prevented. The 20% uncertainty in air core depth is negligible compared to this margin and therefore acceptable for engineering applications. This however, will ask for a clear communication on this point with practitioners. The results of the work presented here will be used to study the ability of the free-surface vortex as a transport mechanism to remove floating debris. The outcome of this research will be published in future communications.

Funding

This experimental research work is financed by the Municipality of Rotterdam, the Netherlands, Deltares, the Netherlands and the Dutch Ministry of Economic Affairs.

Notation

a = gradient of axial velocity (s^{-1})
A = cross-sectional area normal to flow (m^2)

d = pipe diameter, length of quadripod (m)
D = outlet diameter (m)
g = gravitational constant (m s^{-2})
h = height of plane measured from tank bottom (m)
H = undisturbed water depth above outlet (m)
H_D = total surface depression or air core depth (m)
k = constant (–)
n = number of measurement planes (–)
N = number of revolutions (–)
p = pressure (N m^{-2})
q = flow rate per unit of height (m^2 s^{-1})
Q = flow rate (m^3 s^{-1})
Q_v = vortex flow rate (m^3 s^{-1})
r = radial coordinate (m)
r_c = vortex core radius (m)
R = non dimensional radius (–)
R = Reynolds number (–)
R_o = Rossby number (–)
S = submergence depth (m)
t = time (s)
U_o = mean outlet velocity (m s^{-1})
$\boldsymbol{V}$ = vortex velocity field
V_r = radial velocity (m s^{-1})
V_z = axial velocity (m s^{-1})
V_θ = tangential velocity (m s^{-1})
W_e = Weber number (–)
z = axial coordinate (m)
α = bounding radius (m)
δ = relative contribution of surface tension (–)
ε = eddy viscosity (m s^{-2})
ζ = nominal depression slope (–)
θ = azimuthal coordinate (rad)
ν = kinematic viscosity (m s^{-2})
ν_{eff} = effective viscosity (m s^{-2})
ρ = density (kg m^{-3})
σ = surface tension (N m^{-2}), standard deviation
Γ = circulation (m^2 s^{-1})
Ω = angular velocity (rad s^{-1})
ω = vorticity (s^{-1})

References

American National Hydraulic Standards Institute. (2012). *American National Standard for rotodynamic pumps for pump intake design*. ANSI 9.8-2012. ISBN 978-880952-70-2.

Andersen, A., Bohr, T., Stenum, B., Rasmussen, J. J., & Lautrup, B. (2006). The bathtub vortex in a rotating container. *Journal of Fluid Mechanics*, *556*, 121–146.

Anwar, H. O. (1966). Formation of a weak vortex. *Journal of Hydraulic Research*, *4*(1), 1–16.

Anwar, H. O., & Amimilett, M. B. (1980). Vortices at vertically inverted Intake. *Journal of Hydraulic Research*, *18*(2), 123–134.

Anwar, H. O., Weller, J. A., & Amphlett, M. B. (1978). Similarity of free-vortex at horizontal intake. *Journal of Hydraulic Research*, *16*(2), 95–105.

Brocard, D. N., Beauchamp, C. H., & Hecker, G. E. (1983). *Analytic predictions of circulation and vortices at intakes* (Research Project 1199-8). Holden, MA: Alden Research Laboratory (US).

Burgers, J. M. (1948). A mathematical model illustrating the theory of turbulence. *Advances in Applied Mechanics*, *1*, 171–199.

Dagget, L. L., & Keulegan, G. H. (1974). Similitude conditions in free surface vortex formations. *Journal of Hydraulics Division*, *100*, 1565–1581.

Duinmeijer, S. P. A., & Clemens, F. H. L. R. (2016, September). *Experimental research on free-surface vortices as transport mechanism in wastewater sumps*. *Paper presented at the 8th International Conference on Sewer Processes and Networks*, Rotterdam, The Netherlands.

Echávez, G., & McCann, E. (2002). An experimental study on the free surface vertical vortex. *Experiments in Fluids*, *33*, 414–421.

Einstein, H. A., & Li, H. L. (1951). Steady vortex flow in a real fluid. *Proceedings of the Heat Transfer and Fluid Mechanics Institute*, *4*, 33–43.

Gulliver, J. S., & Rindels, A. J. (1987). Weak vortices at vertical intakes. *Journal of Hydraulic Engineering*, *113*, 1101–1116.

Hite, J. E., & Mih, W. C. (1994). Velocity of air-core vortices at hydraulic intakes. *Journal of Hydraulic Engineering*, *120*(3), 284–297.

Ito, K., Ezure, T., & Ohshima, H. (2014). Development of vortex model with realistic axial velocity distribution. *The Japan Society of Mechanical Engineers*, *80*(818), 1–9.

Korving, H., Clemens, F. H. L. R., & van Noortwijk, J. M. (2006). Statistical modeling of the serviceability of sewage pumps. *Journal of Hydraulic Engineering*, *132*, 1076–1085.

Meinhart, C. D., Wereley, S. T., & Santiago, J. G. (2000). A PIV algorithm for estimating time-averaged velocity fields. *Journal of Fluids Engineering*, *122*, 285–289.

Mih, W. C. (1990). Discussion of analysis of fine particle concentrations in a combined vortex. *Journal of Hydraulic Research*, *28*(3), 392–396.

Odgaard, A. J. (1986). Free-surface air core vortex. *Journal of Hydraulic Engineering*, *112*(7), 610–620.

Pennings, P. C., Westerweel, J., & Van Terwisga, T. J. C. (2015). Flow field measurement around vortex cavitation. *Experiments in Fluids*, *56*(11), 1–13.

Rankine, W. J. M. (1858). *Manual of applied mechanics*. London: R. Griffin & Co.

Rindels, A. J., & Gulliver, J. S. (1983). *An experimental study of critical submergence to avoid free-surface vortices at vertical intakes* (Report No. 224). Minneapolis (MN): University of Minnesota (US).

Soloff, S. M., Adrian, R. J., & Liu, Z-C. (1997). Distortion compensation for generalized stereoscopic particle image velocimetry. *Measurement science and technology*, *8*(12), 1441–1454.

Suerich-Gulick, F., Gaskin, S. J., Villeneuve, M., & Parkinson, E. (2014a). Free surface intake vortices: Scale effects due to surface tension and viscosity. *Journal of Hydraulic Research*, *52*(4), 513–522.

Suerich-Gulick, F., Gaskin, S. J., Villeneuve, M., & Parkinson, E. (2014b). Characteristics of free surface vortices at low-head hydropower intakes. *Journal of Hydraulic Engineering*, *140*, 291–299.

Sun, H., & Liu, Y. (2015). Theoretical and experimental study on the vortex at hydraulic intakes. *Journal of Hydraulic Research*, *53*(6), 787–796.

Vatistas, G. H. (1989). Analysis of fine particle concentrations in a combined vortex. *Journal of Hydraulic Research*, *27*(3), 417–427.

Wang, Y., Jiang, C., & Liang, D. (2011). Comparison between empirical formulae of intake vortices. *Journal of Hydraulic Research*, *49*(1), 113–116.

Westerweel, J., & Scarano, F. (2005). Universal outlier detection for PIV data. *Experiments in Fluids*, *39*(6), 1096–1100.